PCCP

PAPER

View Article Online
View Journal | View Issue

Check for updates

Cite this: *Phys. Chem. Chem. Phys.*, 2025, **27**, 5064

Energy transfer booster: how a leaving group controls the excited state pathway within a caging BASHY–BODIPY dyad†

Yagmur Aydogan-Sun, ‡[a] Maximiliane Horz, ‡[a] Rebekka Weber,[b] Myron Heinz,[a] Markus Braun,[a] Alexander Heckel, *[b] Irene Burghardt *[a] and Josef Wachtveitl *[a]

Photocages are powerful tools for spatiotemporal control of molecule release or biological activity. However, many photocages are unsuitable for biological experiments since they are mostly activated by harmful ultraviolet (UV) light and often lack a sufficient optical readout. Thus, there is a high demand for near infrared (NIR) and/or two-photon activatable photocages with a characteristic readout. In this report, we will study a supramolecular, covalently linked energy-transfer dyad based on a **BASHY** fluorophore serving as a two-photon antenna for a poorly two-photon absorbing **BODIPY** photocage. The herein investigated systems, with and without a leaving group (LG), show different excitation energy transfer (EET) efficiencies and therefore differ in their fluorescence properties. To understand the molecular basis for these significant differences, detailed spectroscopic and theoretical analyses were employed from ultrafast transient absorption spectroscopy to excited-state electronic structure calculations and quantum dynamical modelling. The result of our comprehensive study reveals the pivotal role of the LG as an EET booster through specific pathway guidance. In contrast, without the LG, the EET efficiency is reduced and the excitation energy predominantly dissipates within the **BASHY** chromophore. The present study highlights that LGs can actively contribute to optimizing the properties of dyad based systems and offers new design principles for monitoring uncaging *via* an intrinsic fluorescence readout.

Received 18th December 2024,
Accepted 10th February 2025

DOI: 10.1039/d4cp04776a

rsc.li/pccp

Open Access Article. Published on 14 February 2025. Downloaded on 2/20/2026 7:53:16 AM.
This article is licensed under a Creative Commons Attribution 3.0 Unported Licence.

1 Introduction

In recent decades, photocages evolved to an indispensable element for spatiotemporal control of light-driven processes. As an integral part of their structure, photocages usually carry a "caged" molecular unit whose functionality is masked by the photocage. Upon light irradiation this molecular unit, often classified as the leaving group (LG), can be released from the photocage and its activity is restored. While the chromophore represents the light-responsive unit, the LG is typically designed to be the key functional component. Thus, many applications are possible with a single photocage by varying its LG for the desired experimental observation. The applications range from triggering biological activity[1–3] or manipulating it *via* optogenetic approaches[4,5] to medical applications such as drug release[6,7] or photodynamic therapy.[8,9]

Despite these promising applications, photocages are still far from clinical applications, since most of them are only efficiently activated by UV excitation which is harmful to biological tissue. Ideally, photocages would respond within the therapeutic window ranging from 650 to 950 nm, where the penetration into biological tissue is the most effective.[10] However, activation in the red through 1-photon excitation is usually inefficient due to the increase of non-radiative transitions and the lack of energy needed for successful cleavage.[11] Still, many advances were recently made in 1-photon NIR-activatable photocages.[8,12,13] Another possibility for NIR activation is through 2-photon excitation which allows photorelease within the biological window while likely maintaining the uncaging efficiency of UV photocages. Unfortunately, most commonly used photocages inherently exhibit poor 2-photon absorption (2PA)[14] and therefore high excitation intensities are needed due to the squared dependency of 2PA on intensity. On

[a] *Institute for Physical and Theoretical Chemistry, Goethe-University Frankfurt, Max-von-Laue Str. 7, 60438 Frankfurt, Germany. E-mail: wveitl@theochem.uni-frankfurt.de, burghardt@chemie.uni-frankfurt.de*
[b] *Institute for Organic Chemistry and Chemical Biology, Goethe-University Frankfurt, Max-von-Laue Str. 7, 60438 Frankfurt, Germany. E-mail: heckel@uni-frankfurt.de*

† Electronic supplementary information (ESI) available. See DOI: https://doi.org/10.1039/d4cp04776a

‡ These authors contributed equally to this work.

This journal is © the Owner Societies 2025

Open Access Article. Published on 14 February 2025. Downloaded on 2/20/2026 7:53:16 AM.
This article is licensed under a Creative Commons Attribution 3.0 Unported Licence.

the one hand, this allows high spatial resolution, but on the other hand this approach makes the observation of 2-photon activated release challenging owing to the small excitation volume of a few femtoliters. So far, 2-photon uncaging is usually observed by 2-photon fluorescence microscopy and mainly on immobilized samples to avoid diffusion effects. For such experiments biological activity, induced by the LG, typically results in a change of fluorescence properties which is used as the optical readout.[15–17]

Nevertheless, the beneficial properties of 2PA outweigh these challenges and thus there is a high demand for photocages with efficient 2PA capabilities. There are three main strategies to improve 2PA of photocages. One strategy involves structural modifications on the chromophore such as extension of the π-system or attachment of push–pull groups.[14,18] A downside of this strategy is, however, that it typically results in a significant loss of uncaging efficiency since further possible deactivation pathways are introduced. Another, less common strategy, involves refunctioning 2-photon fluorophores into photocages. The benefit of this strategy is that fluorophores are highly optimized molecules with a long-lived excited state, where fast deactivation channels are already eliminated.[19,20] So far, this strategy is not straightforward and involves careful assessment of the structural features and a perfect positioning of the LG for a significant uncaging efficiency. The third strategy is based on cooperative dyad systems where the excitation and uncaging processes are separated onto two molecular units.[21,22] The first unit acts as an antenna, mainly absorbing the excitation light and subsequently transferring it to the functional unit, in this case the photocage. Usually, the antenna is chosen to be a molecule with good 1-photon and 2-photon properties to yield a more efficient excitation process. The details of excitation energy transfer (EET) highly depend on the nature and length of the connecting linker between the two units. While conjugated and flexible linkers lead to supermolecular systems with new properties, non-conjugated and rigid linkers, preferably also in ''meta''-connectivity allow a strong separation of the excitation energy localization and thus preservation of the respective chromophore properties. Therefore, this modular approach offers a variety of possibilities by slight adjustments of the linker design.

In this context, our aim is to enhance the 2PA properties of a photocage without extensive derivatization of its chromophore. To this end, we developed a dyad based on **BASHY** and **BODIPY** featuring an energy transfer between the two moieties (see Fig. 1A). While **BODIPY** is known to be an excellent fluorophore,[23] since its discovery many decades ago, in recent years it has also evolved as an important photocage.[24] Meanwhile, **BASHY** was introduced in 2016 in a collaborative work of the Pischel and Gois labs.[25] Despite having similarly advantageous properties as **BODIPY** and even featuring intrinsically good 2PA for the basic chromophore,[26] **BASHY** still finds little usage by the majority of the community. In this work, we present two **BASHY–BODIPY** dyads, where **BASHY** serves as a 2P antenna for the poorly 2-photon absorbing **BODIPY**

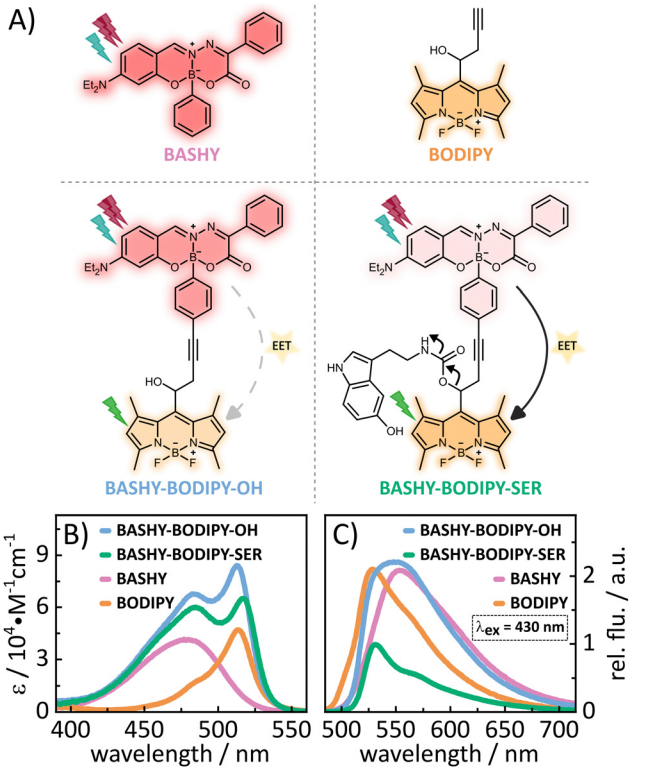

Fig. 1 (A) Molecular structures of the investigated chromophores and the two investigated dyads with different residues (OH, SER), their respective contribution to emission and excitation energy transfer (EET) efficiency are indicated. Additional arrows in the structure of **BASHY–BODIPY–SER** indicate the uncaging process *via* decarboxylation of the carbamate linker. (B) Absorption spectra in DMSO plotted against the extinction coefficient. (C) Fluorescence spectra in DMSO analyzed in relation to their fluorescence quantum yield.

photocage. In both dyads, the two moieties are covalently bound through a rigid alkyne linker. The only difference between the two dyads is the mesomethyl position of **BODIPY** where one dyad (**BASHY–BODIPY–SER**) bears serotonin (**SER**) as a leaving group and the other one (**BASHY–BODIPY–OH**) carries a hydroxy group instead. Interestingly, while this seems to be a small difference at first sight, the leaving group has an impact not only on the fluorescence properties (see Fig. 1C), but also on the excited state dynamics and especially the energy transfer efficiency. Notably, this behavior was previously observed in another dyad with the same linker construction.[27] In order to understand the cause of these remarkable differences, both dyads as well as the respective single chromophores **BASHY** and **BODIPY** were subjected to detailed spectroscopic and theoretical analyses. The structures of the investigated molecules are displayed in Fig. 1A and their syntheses are presented in the ESI.†

2 Results and discussion

2.1 Steady state properties

A lot of information about the electronic coupling and the EET efficiency within a dyad can be obtained from the stationary

Open Access Article. Published on 14 February 2025. Downloaded on 2/20/2026 7:53:16 AM. This article is licensed under a Creative Commons Attribution 3.0 Unported Licence.

properties of the dyad and its individual chromophore units. Thus, in the following a detailed discussion of the absorption (Fig. 1B) and fluorescence (Fig. 1C) properties is provided. Regarding the steady state properties of the single chromophores, **BODIPY** shows a more redshifted absorption, while its fluorescence is more blueshifted compared to **BASHY**. This reflects a large difference in their Stokes shifts. While **BODIPYs** generally show small Stokes shifts, **BASHYs** tend to have a larger, highly solvent-dependent Stokes shift. In polar solvents such as DMSO, **BASHYs** display a strong intramolecular charge transfer (ICT) character in the excited state (see Fig. S17, ESI† and ref. 25). This ICT state can be stabilized by polar solvents, resulting in a redshift and a reduction in fluorescence efficiency. The absorption spectra of both dyads resemble the sum of the single chromophores' absorption spectra. This preservation of the respective building block properties indicates a localization of the excited states on either one or the other chromophore. Another important aspect of energy-transfer systems like dyads is their fluorescence spectra since the amount of fluorescence from either the donor or the acceptor state will indicate how efficient the EET is. The fluorescence spectra of the two dyads differ significantly, as can be seen in Fig. 1C. While **BASHY–BODIPY–OH** seems to show a mixed fluorescence from both states, the fluorescence in **BASHY–BODIPY–SER** completely results from the **BODIPY** state. Thus, the EET within **BASHY–BODIPY–OH** seems to be less efficient compared to **BASHY–BODIPY–SER**. The leaving group **SER**, as the only remarkable difference between both dyads, apparently facilitates the energy transfer. Given that **SER** is a relatively large leaving group, capable of forming a hydrogen bond with the fluorine atoms of **BODIPY** (see Fig. S2, ESI†), we initially hypothesized that this interaction might play a key role in the divergent EET efficiencies. However, our investigation of another dyad **BASHY–BODIPY–AC**, with acetic acid as the LG (see Fig. S18, ESI†), which exhibits similar EET efficiency to **BASHY–BODIPY–SER**, showed that the observed behavior cannot be solely attributed to the hydrogen bonding. Furthermore, the leaving group also appears to affect the fluorescence quantum yield, as shown for **BASHY–BODIPY–SER** in Table 1. While with 22%, **BASHY–BODIPY–OH** preserves the fluorescence quantum yield of the individual chromophores, the fluorescence quantum yield of **BASHY–BODIPY–SER** drops to 10%. Such a significant drop can be caused by a photoinduced electron transfer (PET) from the **BODIPY** to the LG.[28] Another possibility is that the fluorescence becomes less efficient as other competing pathways like uncaging increase.

Table 1 Fluorescence quantum yields and extinction coefficients at the respective maxima in DMSO. While 484 nm represents the absorption maximum of **BASHY**, the 514 nm mainly consists of **BODIPY** absorption

Molecule	ϕ_f (%)	ε_{484nm} (cm^{-1} M^{-1})	ε_{514nm} (cm^{-1} M^{-1})
BASHY	21	41 000 ± 500	11 700 ± 100
BODIPY	21	17 240 ± 120	47 000 ± 200
BASHY–BODIPY–OH	22	67 300 ± 400	84 000 ± 400
BASHY–BODIPY–SER	10	58 300 ± 900	65 000 ± 700

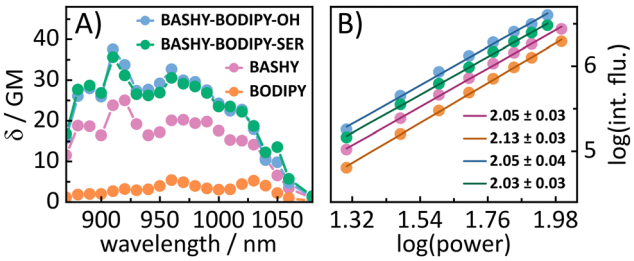

Fig. 2 (A) 2P excitation spectra of the molecules in DMSO obtained by the 2P induced fluorescence method. (B) Power squared dependence of the 2P induced fluorescence.

In addition to the one-photon absorption properties, the 2P excitation spectra for all four molecules (see Fig. 2A) were recorded using 2-photon induced fluorescence in order to verify the improved 2P excitability of **BODIPY** within the dyads. All molecules show power squared dependence (see Fig. 2B) within the measured power range (see the ESI† for details of the experimental settings). In accordance with the literature,[29] **BODIPY** shows low 2PA over the whole measured wavelength range. The highest obtained value for **BODIPY** is 5 GM at 960 and 1030 nm. **BASHY** on the other hand is known to be a better 2P absorber and shows 2PA cross-sections of 25 GM at 920 nm and 20 GM at 970 nm, which are assigned to a vibrational feature and the maximum of the S_1 transition. Notably, this vibrational feature aligns well with the one observed in the steady-state absorption spectrum with toluene (see Fig. S17, ESI†). In general, these values are in the range expected for the basic **BASHY** chromophore.[30] **BASHY–BODIPY–OH** shows 2PA cross-sections of 37 GM at 910 nm and 32 GM at 960 nm, while **BASHY–BODIPY–SER** exhibits slightly lower values of 35 GM at 910 nm and 30 GM at 960 nm. Thereby, they not only compensate the low 2PA cross-sections of **BODIPY** but even enhance the 2P excitability of **BASHY**. Small contributions of **BODIPY** to the 2PA of the dyads are noticeable at 960 and 1050 nm.

For a more detailed insight into the excited state properties, electronic structure calculations employing density functional theory (DFT) and its time-dependent extension (TD-DFT) as implemented in the Gaussian16 package were performed for the dyads and their molecular components **BODIPY** and **BASHY**.[31] The ground state equilibrium structures of the single chromophores **BASHY** and **BODIPY** as well as of both dyads were obtained using the long-range corrected CAM-B3LYP functional[32] and Ahlrich's def2-SVP double-zeta basis set.[33,34] These geometries were confirmed to be minima *via* a subsequent harmonic vibrational analysis. Excited state properties, *i.e.*, vertical excitation energies, oscillator strengths *f*, transition dipole moments and density differences were obtained within the adiabatic approximation employing the same functional and basis set combination. Solvent effects of DMSO were accounted for using the polarizable continuum model (PCM).[35–37] Analysis of the state character was obtained *via* the TheoDORE tool where electron–hole maps are constructed from fragment-based transition densities.[38–40]

 This journal is © the Owner Societies 2025

Open Access Article. Published on 14 February 2025. Downloaded on 2/20/2026 7:53:16 AM.
This article is licensed under a Creative Commons Attribution 3.0 Unported Licence.

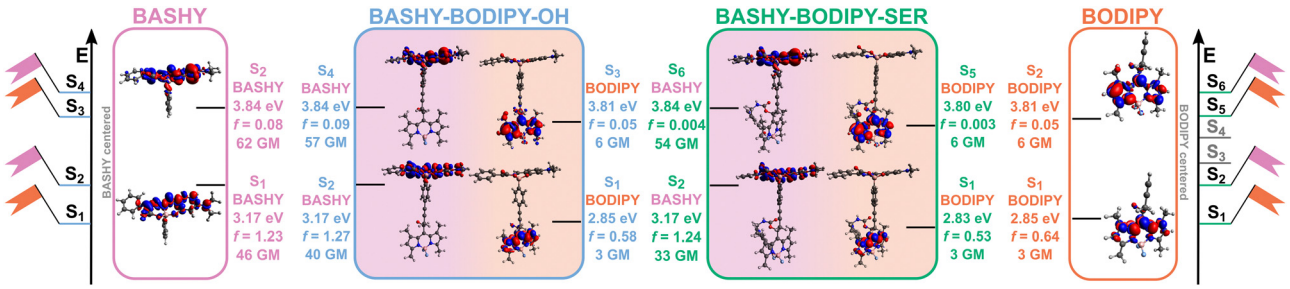

Fig. 3 Electron density differences for the relevant locally excited states of both the dyad with and without the additional leaving group serotonin. Excited states of the isolated moieties **BODIPY** and **BASHY** are depicted for comparison. Localization of an excited state within the molecular dyads on a specific fragment is indicated.

The excited state analysis of **BASHY–BODIPY–OH** and **BASHY–BODIPY–SER** is reported in Fig. 3 and Table 2. The state ordering is very similar between the two dyads with **BASHY–BODIPY–OH** displaying two one-photon bright states with excitation energies of 2.85 eV (435 nm) and 3.17 eV (391 nm), followed by two spectroscopically dark states at 3.81 eV (325 nm) and 3.84 eV (323 nm), while **BASHY–BODIPY–SER** features two bright states at 2.83 eV (438 nm) and 3.17 eV (391 nm), followed by four dark states at 3.19 eV (389 nm), 3.65 eV (340 nm), 3.80 eV (327 nm) and 3.84 eV (323 nm). Corresponding to the spectroscopic indications, the excited states are mostly localized on either of the two moieties, with the S_1 state being localized on the **BODIPY** fragment and the S_2 state on the donor **BASHY** moiety. While both excited states are localized on either moiety of the dyad, the first **BASHY** excitation is known to exhibit an ICT character on the **BASHY** fragment as previously observed by experimental and computational analyses.[41–43] This ICT character is reflected in a shift of the density from the outer part of the big π-system and the diethylamine-substituent to the center of the **BASHY** scaffold, which is facilitated by the planarization of the benzyl-substituent with regard to the rest of the π-system upon photoexcitation (see Fig. S5, ESI†). A detailed partitioning for the ICT analysis based on the TheoDORE tool can be found in Fig. S7 in the ESI.†

Table 2 Excited state energies, oscillator strengths, two-photon cross-sections as well as an indication of the character for the relevant states of **BASHY–BODIPY–OH** and **BASHY–BODIPY–SER**, respectively, using the CAM-B3LYP functional and def2-SVP basis. ICT numbers are obtained *via* TheoDORE and defined in the ESI. States marked in italics play no important role in an initial excitation *via* either one- or two-photon absorption and in the case of **BASHY–BODIPY–SER** refer to intermediate ICT states localized on the **BODIPY** moiety that might be involved in later uncaging processes. In the case of **BASHY–BODIPY–OH** they describe higher-lying states

	System	BASHY–BODIPY–OH	BASHY–BODIPY–SER
S_1	Excitation energy (eV)	2.85	2.85
	Oscillator strength f	0.58	0.53
	σ_{2P} (GM)	3	3
	Character (ICT number)	LE_{BODIPY} (0.035)	LE_{BODIPY} (0.038)
S_2	Excitation energy (eV)	3.17	3.17
	Oscillator strength f	1.27	1.24
	σ_{2P} (GM)	40	33
	Character (ICT number)	ICT_{BASHY} (0.462)	ICT_{BASHY} (0.469)
S_3	Excitation energy (eV)	3.81	*3.19*
	Oscillator strength f	0.003	*0.003*
	σ_{2P} (GM)	6	*0.06*
	Character (ICT number)	LE_{BODIPY} (0.033)	*ICT_{BODIPY} (0.994)*
S_4	Excitation energy (eV)	3.84	*3.65*
	Oscillator strength f	0.09	*0.0004*
	σ_{2P} (GM)	57	*0.4*
	Character (ICT number)	ICT_{BASHY} (0.530)	*ICT_{BODIPY} (0.996)*
S_5	Excitation energy (eV)	*4.08*	3.80
	Oscillator strength f	*0.08*	0.003
	σ_{2P} (GM)	*23*	6
	Character (ICT number)	*ICT_{BASHY} (0.244)*	LE_{BODIPY} (0.036)
S_6	Excitation energy (eV)	*4.11*	3.84
	Oscillator strength f	*0.05*	0.004
	σ_{2P} (GM)	*4*	54
	Character (ICT number)	*LE_{BODIPY} (0.045)*	ICT_{BASHY} (0.530)

The description of **BASHY** in the dyad setup is in accordance with this established ICT character, indicated by an ICT_{BASHY} label in Table 2. Corresponding to previous computational investigations, the ICT **BASHY** state is mainly described *via* a HOMO → LUMO transition,[41,42] and further analysis of natural transition orbitals (NTOs) for the **BASHY** localized states can be found in Fig. S6 in the ESI.†

Following the first two excited states **BASHY–BODIPY–SER** exhibits two intermediate dark states at 3.19 eV (389 nm, $f = 0.003$) and 3.65 eV (340 nm, $f = 0.0004$) that are not present in **BASHY–BODIPY–OH**. These are localized on **BODIPY** and **SER** and display a strong ICT character. While they do not play any role in the initial excitation due to the negligible accessibility at the Franck–Condon (FC) geometry, they likely contribute to the uncaging following the energy transfer as discussed by various mechanistic studies.[44,45] Accordingly, the S_3 state of **BASHY–BODIPY–OH** corresponds to the S_5 state of **BASHY–BODIPY–SER** which is again localized on the acceptor **BODIPY** fragment and the S_4 state of **BASHY–BODIPY–OH** matches the S_6 state of **BASHY–BODIPY–SER** and is another **BASHY**-centered state for both dyads. The respective excited states exhibit the same contributions of orbital transitions and in general display similar properties when compared to the molecular compounds of **BASHY** and **BODIPY** as can be seen in Fig. 3 and in the ESI† (Fig. S3 and S4). This is mainly a consequence of the non-conjugated and rigid alkyne linker placed between the two fragments that prevents strong electronic coupling or stacking interactions. Moreover, the orbital transitions involved in the

Open Access Article. Published on 14 February 2025. Downloaded on 2/20/2026 7:53:16 AM.
This article is licensed under a Creative Commons Attribution 3.0 Unported Licence.

lowest-lying singlet excitations of **BODIPY** and **BASHY** confirm the observed differences regarding the ICT character with **BODIPY** displaying locally excited (LE) states and **BASHY** featuring a stronger redistribution of electron density across the scaffold upon photoexcitation (see Fig. S3–S6 in the ESI†).

Complementary to the measurements, the 2PA cross-sections σ_{2P} were computed employing a sum-over-states expression within a quadratic response scheme as implemented in DALTON using the CAM-B3LYP functional and def2-SVP basis set.[46] The 2P activities of the respective states are indicated in Fig. 3 and confirm the accessibility of the dyads *via* 2P excitation. As demonstrated by the experimental measurements, there is a significant difference in the 2PA cross-sections of **BODIPY** and **BASHY**, which is reproduced by the simulated 2PA cross-sections. **BODIPY** exhibits a σ_{2P} of 3 GM for the S_1 state and 6 GM for the S_2 state while the cross-sections of **BASHY** generally range from 40 GM to 60 GM. The 2P active states in the dyads correspond to the **BASHY**-centered states and upon introduction of the LG the cross-sections are slightly decreased. In general, the calculated and experimental 2PA values for the S_1 transitions of **BASHY** and **BODIPY** and their corresponding match in the dyads (S_1 and S_2 state, respectively) show good agreement. It should be noted that in the 2PA experiments, we only measured within the range of the S_1 transition of **BASHY** and **BODIPY**. However, our calculations suggest that the S_2 transition of **BASHY** should exhibit higher 2-photon activity and approximately lie around 800 nm. Indeed, Pischel, Gois and their coworkers demonstrated in a previous publication that **BASHY** is highly 2-photon active in this wavelength region,[30] further validating our calculations.

Considering the assignments above, the following picture of the photochemical response to the initial excitation emerges: upon irradiation with a UV/vis pulse the target state of the excitation is dependent on the wavelength as either the S_2 state localized on the **BASHY** fragment or the S_1 state on the **BODIPY** fragment is addressed. Upon irradiation with a NIR pump pulse, the dyad is directly excited to one of the **BASHY**-centered states, either the S_2 state or the higher lying S_4/S_6 state, which possibly leads to an initial excitation into a superposition state. This excitation to higher lying singlet states is followed by internal conversion to the S_2 state within the **BASHY** fragment and a subsequent EET to the **BODIPY**-centered S_1 state. In general, these steps are not necessarily sequential and may exhibit temporal overlap, especially if the initial excitation is not strictly limited to one state.

2.2 fs-time-resolved dynamics

To gain further insight into the dynamics of the respective dyads, we performed ultrafast UV/vis transient absorption measurements to investigate the EET in a time-resolved manner. To ensure that we primarily address the energy-transfer from **BASHY** to **BODIPY**, an excitation wavelength of 420 nm was chosen, since the absorption of **BODIPY** for this wavelength is negligible. The obtained time-resolved maps as well as the lifetime density analyses of the dyads and the individual chromophores are shown in Fig. 4. While **BASHY** was also

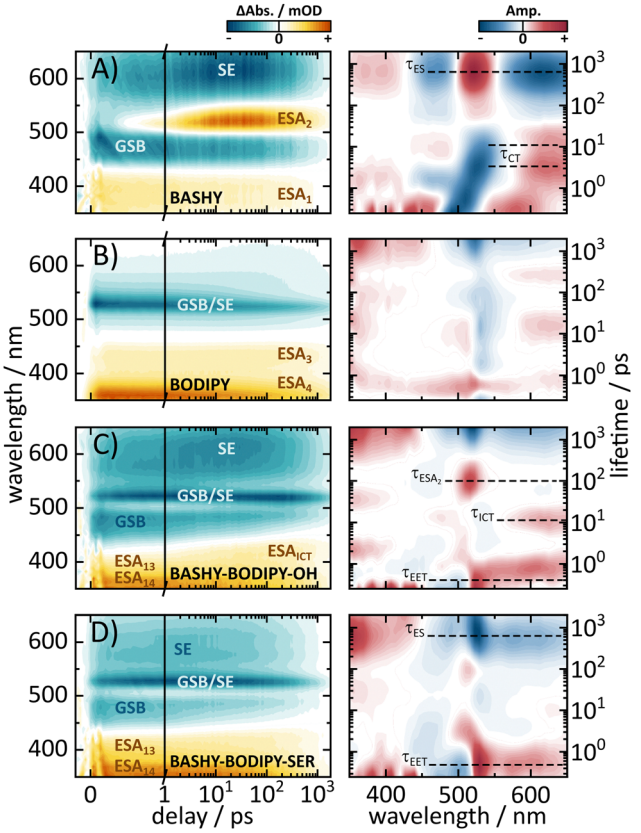

Fig. 4 Transient absorption spectra (left) and the corresponding lifetime density maps (right) for (A) **BASHY**, (B) **BODIPY**, (C) **BASHY–BODIPY–OH** and (D) **BASHY–BODIPY–SER**, measured in DMSO. **BASHY** and the two dyads were excited at 420 nm, where basically no **BODIPY** absorption is present. Thus, **BODIPY** itself was excited at 525 nm. The various transient signals as well as the characteristic lifetimes are labeled with the corresponding processes and will be further explained in the main text.

excited at 420 nm, the **BODIPY** map was measured with an excitation wavelength of 525 nm. Starting with **BASHY**, the single chromophore shows a negative band around 465 nm, assigned to its ground state bleaching (GSB) from the S_1 state, which decays with an approximate lifetime of 800 ps. Similar to **BASHY**'s GSB, the excited state around 370 nm (ESA_1) is already populated within the IRF of the experiment. This indicates that ESA_1 originates from the locally excited S_1 state of **BASHY**. Furthermore, the lack of any spectral shift in ESA_1 over time suggests that it is associated with the more localized, initial excited state rather than the charge-transfer state that forms later due to solvent stabilization. The most recognizable signatures of **BASHY** are ESA_2 around 510 nm and its broad stimulated emission (SE) ranging from 500 nm to 650 nm and beyond. The initial SE from the locally excited S_1 state is centered at 510 nm. Within the first 20 ps the SE shows a strong bathochromic shift, which can be described by two lifetimes. The first lifetime describes the rise of the SE and its initial shift within 500 fs, while the second lifetime around 3–4 ps describes the increase of the SE intensity in the red region. The SE shift lasts till 20–30 ps, which is visible from the extension of the second lifetime into a few tens of ps. These two

 This journal is © the Owner Societies 2025

Open Access Article. Published on 14 February 2025. Downloaded on 2/20/2026 7:53:16 AM.
This article is licensed under a Creative Commons Attribution 3.0 Unported Licence.

lifetimes also contribute to the rise of ESA_2 which presumably emerges due to the shift of the SE. The strong Stokes shift of the SE is characteristic for molecules with a strong ICT character like **BASHY**. It should be noted that the fluorescence maximum of **BASHY** in DMSO is located around 555 nm. However, in the transient maps, the strongest emission appears to be around 610 nm. This discrepancy is caused by the positive contribution of ESA_2 on the short wavelength side of the SE which leads to compensation of the negative SE signal.

In contrast to **BASHY**, **BODIPY** has only one negative band (GSB/SE) around 525 nm which is most likely a combined contribution of its GSB and SE due to its small Stokes shift. The GSB/SE appears to have a blueshift from 530 nm to 523 nm which can be attributed to a contribution of an underlying ESA since GSBs cannot exhibit any shift, while SEs only shift into the red. In the lifetime density map (LDM), this blueshift is represented by broadly distributed lifetimes around 530 nm, resulting in multi-exponential decay dynamics. Around 600 nm a slight shift of GSB/SE into the red (Fig. 4B) occurs which is likely a redshift of the SE component of GSB/SE. This shift is described with a positive amplitude of a 20 ps lifetime in the LDM. Within the observed time-frame, the ground state is not fully recovered yet, but additional time-correlated single photon counting (TCSPC) experiments revealed an excited-state lifetime of 2.1 ns (Fig. S20, ESI†). **BODIPY** also features two ESAs, which are termed ESA_3 and ESA_4. Both ESAs decay with the same lifetime as GSB/SE.

Overall, **BODIPY** and **BASHY** both show pronounced excited state features which are used in the following to distinguish their contributions within the dyads.

Similar to the steady state fluorescence measurements, **BASHY–BODIPY–OH** shows mixed signatures of **BASHY** and **BODIPY**. While the **BODIPY** GSB/SE rises in amplitude within a few femtoseconds, the **BASHY** GSB decays with the same time constant. This behavior can be attributed to an energy transfer from the **BASHY** to the **BODIPY** chromophore. According to the LDM (Fig. 4C, right), this energy transfer happens within 750 fs. Beyond the energy transfer, **BASHY–BODIPY–OH** shows complex dynamics around 522 nm, which is more visible when a single transient at 522 nm (Fig. 5C) is compared with the transient of ESA_2 (Fig. 5A) in **BASHY**. After the initial EET in **BASHY–BODIPY–OH**, this transient shows a decay between 2 and 20 ps. On the same timescale a strong amplitude increase of ESA_2 in **BASHY** occurs. Since ESA_2 has a positive amplitude, it is assumed that an overlap with GSB/SE in **BASHY–BODIPY–OH** leads to an overall decrease of the negative amplitude causing the decay of the transient at this timescale. Then once more, GSB/SE shows an increase in its intensity until 120 ps, which is roughly described by a lifetime of 100 ps in the LDM (Fig. 4C, right). On approximately the same timescale, ESA_2 in **BASHY** (Fig. 5A) starts to decay which in turn leads to an increase of the negative amplitude in **BASHY–BODIPY–OH**. Around 600 ps, the decay of GSB/SE develops, but similar to the **BODIPY** chromophore, the ground state is not fully recovered within the time-frame of the measurement. Also here, additional TCSPC experiments depicted an excited-state

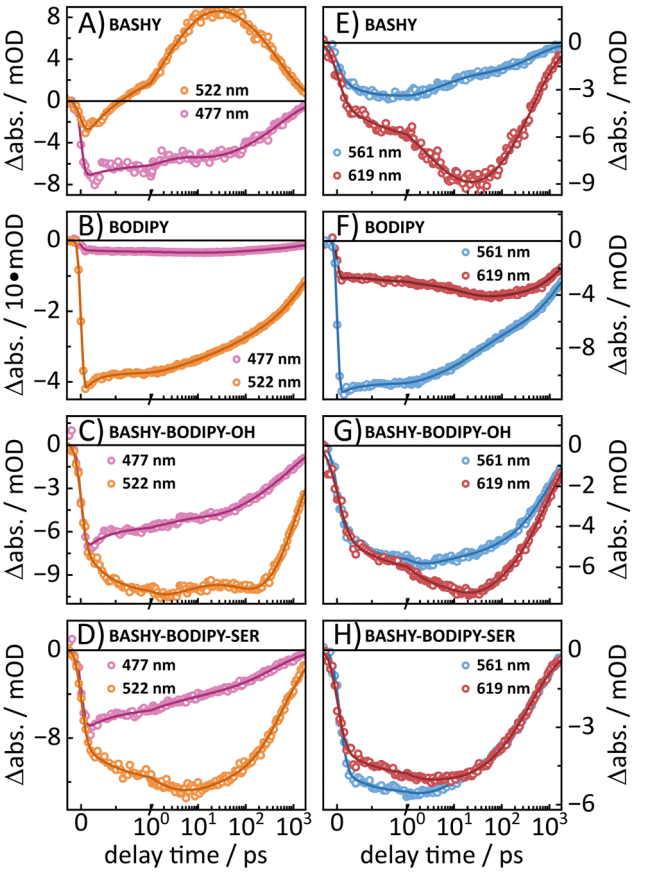

Fig. 5 On the left side the transients at 477 nm and 522 nm are presented for (A) **BASHY**, (B) **BODIPY**, (C) **BASHY–BODIPY–OH** and (D) **BASHY–BODIPY–SER**. The transients at 477 nm of **BASHY** and the two dyads mainly resemble the GSB of the **BASHY** moiety, while **BODIPY** also shows some residual GSB at this wavelength. The transient at 522 nm resembles ESA_2 in **BASHY** and GSB/SE in **BODIPY**. In **BASHY–BODIPY–OH** this 522 nm transient features signatures from both chromophores, while in **BASHY–BODIPY–SER** only GSB/SE seems to be dominant. On the right side, transients of the SE are presented at two distinct wavelengths (561 nm and 619 nm) to visualize the shift of the SE. While (E) **BASHY** as well as (G) **BASHY–BODIPY–OH** both show a strong amplitude increase of the 619 nm transient until 20–30 ps, (F) **BODIPY** only shows a slight increase between 10–80 ps. Contrary to this, (H) **BASHY–BODIPY–SER** shows no pronounced shift at all. The raw data of the transients are marked as dots, while the respective fits are presented by solid lines.

lifetime of 1.4 ns for **BASHY–BODIPY–OH** (Fig. S20, ESI†). Conveniently, this excited-state lifetime lies exactly in between the two parent chromophores **BASHY** (800 ps) and **BODIPY** (2.1 ns), which further confirms the bisected behavior. ESA_{13} and ESA_{14} closely resemble the ESAs of **BODIPY** while an underlying ESA_1 contribution from the **BASHY** chromophore is highly likely. The most noticeable difference of **BASHY–BODIPY–OH**, compared to the parent chromophores, is a new ESA_{ICT}, which is more apparent at later delay times around 420 nm. The LDM shows that this ESA_{ICT} starts to shift at least from 520 nm downwards, as can be seen from the diagonal evolution of a positive amplitude trace starting at 520 nm. This large blue-shift of ESA_{ICT} fits well with the intramolecular charge-transfer stabilization of the **BASHY** chromophore, hence

Open Access Article. Published on 14 February 2025. Downloaded on 2/20/2026 7:53:16 AM. This article is licensed under a Creative Commons Attribution 3.0 Unported Licence.

the name ESA_{ICT}. The initial position of ESA_{ICT} strongly overlaps with **BODIPY**'s GSB/SE and **BASHY**'s GSB, which is why it seems that both signatures shift towards each other once the underlying contribution of ESA_{ICT} vanishes. On later delay times, ESA_{ICT} leads to a partial compensation of **BASHY**'s GSB on the blue side. Further evidence for the strong ICT stabilization of the **BASHY** chromophore within **BASHY–BODIPY–OH** is the quite significant shift of **BASHY**'s SE with a lifetime of 10 ps. The shift of the SE is more apparent when transients of the SE at two different wavelengths are plotted together (Fig. 5G). Compared to the pure **BASHY** (Fig. 5E), **BASHY–BODIPY–OH** shows a similar evolution of the transients as can be seen by the amplitude increase of the 617 nm SE transient up to 20–30 ps. The dyad and the parent **BASHY** chromophore only differ in their excited state lifetimes and their relative ratio of the SE transients. The shifts of ESA_{ICT} and SE indicate that despite the fast EET, a significant amount of the population still dissipates within the **BASHY** chromophore.

Similar to **BASHY–BODIPY–OH**, **BASHY–BODIPY–SER** shows both GSB of **BASHY** and GSB/SE of **BODIPY**. The **BODIPY** GSB/SE signal increases until 2–3 ps, then remains constant until 10 ps, when it starts to decay (Fig. 5D). This constant regime indicates an equilibrium where the rate of energy transfer is equal to the decaying rate of the **BODIPY** moiety. The GSB signal of **BASHY** in **BASHY–BODIPY–SER** (Fig. 5D) on the other hand decays faster compared to the single **BASHY** chromophore (Fig. 5A). This signal pattern can be attributed to an EET as well. According to the LDM the energy transfer occurs mainly with a lifetime of 1–2 ps, which appears to be slightly slower than **BASHY–BODIPY–OH** (Fig. 4D right). After the energy transfer, **BODIPY**'s GSB/SE appears to have a slight blue shift in **BASHY–BODIPY–SER** as well, which is described by a lifetime of 5–20 ps, where a positive amplitude is followed by a red shifted negative amplitude. At the end, both chromophore parts decay with a lifetime of 700–800 ps. Therefore, **BASHY–BODIPY–SER** has apparently a shorter excited state lifetime than **BASHY–BODIPY–OH**. This behavior, additionally to the fluorescence quantum yields, further supports the prior suggested quenching effect of the leaving group. As seen from the transients in Fig. 5H, **BASHY–BODIPY–SER** does not show any significant SE shift and thus, the 10 ps lifetime for the SE shift is missing in the LDM of **BASHY–BODIPY–SER**. As in the case of **BASHY–BODIPY–OH**, ESA_{13} and ESA_{14} also resemble the ESAs of **BODIPY**. But unlike **BASHY–BODIPY–OH**, there is no visible ESA_{ICT} in **BASHY–BODIPY–SER**. The missing ESA_{ICT} as well as the absence of a SE shift indicate that the excitation energy predominately remains within the **BODIPY** chromophore from where the majority of the dynamics take place.

To further investigate the differences between the two dyads, the possibility of a reverse energy transfer from **BODIPY** to **BASHY** was investigated. Due to the short distance between the two chromophores and the close proximity of the energetic levels, a reverse energy transfer is conceivable. For this purpose, additional transient absorption measurements of the two dyads at two other excitation wavelengths were conducted (Fig. S20, ESI†). Thereby, an excitation wavelength of 490 nm was used to address both chromophores equally, whereas 525 nm was used to mainly excite the **BODIPY** chromophore. As expected, by shifting the excitation wavelength towards increasing **BODIPY** absorption, the **BODIPY** dynamics are present with the initial excitation, without the need of an EET. The overall signal patterns are the same as for an excitation with 420 nm despite the more pronounced **BODIPY** contribution. For an excitation at 525 nm, the transient signatures in both **BASHY–BODIPY–OH** and **BASHY–BODIPY–SER** are dominated by the **BODIPY** chromophore. Yet a small **BASHY** population is present from the start, noticeable from the GSB at 485 nm in both dyads and the underlying ESA_2 contribution in **BASHY–BODIPY–OH**, which is attributed to the residual **BASHY** absorbance at the excitation wavelength. Overall, these results further emphasize that the properties of the components are preserved and that the excitation energy is transferred predominantly *via* a relatively weak electronic coupling between the two chromophores.

2.3 Quantum dynamical EET analysis

The dyad systems under study bear strong analogies to the **rhodamine(RHO)–BODIPY** dyad which was recently investigated by some of us.[47] Due to the spatial extension of the donor and acceptor moieties and the ultrafast character of the EET dynamics, a computational treatment beyond the standard Förster theory is required.[48] Therefore, our previous analysis combined the computation of electronic couplings by a transition density analysis with high-dimensional quantum dynamics in the full normal-mode space.[47] Importantly, we found that the EET step, on a time scale around 100 fs, is of coherent character, and a superposition of donor and acceptor states persists on a picosecond scale. For the present **BASHY–BODIPY** systems, we choose a similar approach while anticipating that the EET time scale will be longer.

Quantum dynamical simulations were performed for both dyads employing the multi-layer multiconfiguration time-dependent Hartree (ML-MCTDH) method[49–51] in combination with a linear vibronic coupling (LVC) Hamiltonian[52] and including the full set of normal modes (N = 264 for **BASHY–BODIPY–OH** and N = 339 for **BASHY–BODIPY–SER**). We focus on initial excitation to the **BASHY**-centered S_2 state; excitation to higher-lying states would necessitate including internal conversion dynamics. The Hamiltonian comprises two diabatic fragment-based states *i.e.*, the ICT state on the donor (**BASHY**) moiety, labeled $|ICT^D\rangle$, and the locally excited state on the acceptor (**BODIPY**) moiety, labeled $|LE^A\rangle$

$$\begin{aligned}\hat{H} = &\sum_{i=1}^{N}\Big(\frac{\omega_i}{2}(\hat{q}_i^2+\hat{p}_i^2)+\kappa_{i,ICT^D}\hat{q}_i|ICT^D\rangle\langle ICT^D| \\ &+\kappa_{i,LE^A}\hat{q}_i|LE^A\rangle\langle LE^A|\Big) \\ &+j_{DA}\big(|LE^A\rangle\langle ICT^D|+|ICT^D\rangle\langle LE^A|\big) \\ &+\Delta E|ICT^D\rangle\langle ICT^D|\end{aligned} \tag{1}$$

where $\hat{q}_i$ is the position operator, $\hat{p}_i=-i\hbar\frac{\partial}{\partial q_i}$ is the corresponding momentum operator and mass and frequency

 This journal is © the Owner Societies 2025

Open Access Article. Published on 14 February 2025. Downloaded on 2/20/2026 7:53:16 AM.
This article is licensed under a Creative Commons Attribution 3.0 Unported Licence.

weighted coordinates are used. Furthermore, κ_i denote the vibronic couplings, j_{DA} the electronic coupling constant and ΔE the electronic offset between donor and acceptor state. Due to the small electronic coupling between the fragments, the diabatic energy gap is approximated by the adiabatic gap between the S_1 and S_2 states from our supermolecular calculations. The strong localization of the excited states further suggests the use of fragment-based normal modes. This includes N_D = 147 modes on the **BASHY** moiety and either N_A = 117 (**OH**) or N_A = 192 (**SER**) on the **BODIPY** fragment. The vibronic coupling constants are obtained as the projection of the gradient of the two excited states at the FC geometry onto the respective ground state normal modes.[53] With the excited states showing strong localization, the vibronic couplings of a given state only contribute significantly in combination with the normal modes localized on the same fragment (Fig. S10–S13, ESI†). From the vibronic couplings, the reorganization energies $\lambda = \sum_i (\kappa_i^2/2\omega_i)$ are obtained, yielding λ_D = 0.26 eV for the ICT state on the **BASHY** moiety and λ_A = 0.05 eV for the LE state on the **BODIPY** moiety.

The electronic coupling j_{DA} is obtained *via* the EET implementation in Gaussian16 including a solvent description.[54] Transition densities are used to obtain exchange and overlap interaction terms alongside the Coulombic effect and solvent effects are introduced *via* the integral equation formalism (IEF) version of the PCM

$$j_{DA} = \iint \rho_D^{*el}(\vec{r}_d)\left(\frac{1}{|\vec{r}_d - \vec{r}_a|} + \frac{\partial^2 E_{XC}[\rho^{el}]}{\partial\rho^{el}(\vec{r}_d)\partial\rho^{el}(\vec{r}_a)}\right)\rho_A^{el}(\vec{r}_a)\mathrm{d}\vec{r}_d\mathrm{d}\vec{r}_a + \sum_k \left(\int \rho_D^{*el}(\vec{r}_a)\frac{1}{|\vec{r}_a - s_k|}\mathrm{d}\vec{r}_a\right) q(s_k;\varepsilon_\omega,\rho_A^{el}) - \omega_0 \int \rho_D^{*el}(\vec{r}_a)\rho_A^{el}(\vec{r}_a)\mathrm{d}\vec{r}_a \quad (2)$$

with the transition densities $\rho_D^{el}(\vec{r}_d) = \Psi_{D_g}(\vec{r}_d)\Psi_{D_e}^*(\vec{r}_d)$ and $\rho_A^{el}(\vec{r}_a) = \Psi_{A_g}(\vec{r}_a)\Psi_{A_e}^*(\vec{r}_a)$, where Ψ_{D_g}, Ψ_{D_e}, Ψ_{A_g} and Ψ_{A_e} are the donor and acceptor ground (g) and excited state (e) wavefunctions, $\vec{r}_a$ and $\vec{r}_d$ are the electron coordinates on the respective fragment, $E_{XC}[\rho^{el}]$ is the exchange correlation functional, s_k is the center of the discrete elements of the solvent cavity surface, ε_ω the respective dielectric constant of the chosen solvent and q represents the point charges placed at the center of the solvent cavity elements.

As the rotational potential around the linker axis is expected to exhibit low barriers due to the restrictive geometry of the bridged scaffold, a ground state relaxed potential energy surface (PES) scan was conducted (see Fig. S1, ESI†) in both cases. This revealed that the **BASHY–BODIPY–OH** dyad is freely rotatable, while the **BASHY–BODIPY–SER** dyad exhibits a slight preference for parallel-oriented structures. Since the different rotational conformations in the case of **BASHY–BODIPY–SER** can have some influence on the timescale of the EET, three different rotamers (**–SER1**, **–SER2**, **–SER3**) are considered for the subsequent quantum dynamical analysis (see Fig. S2, ESI†).

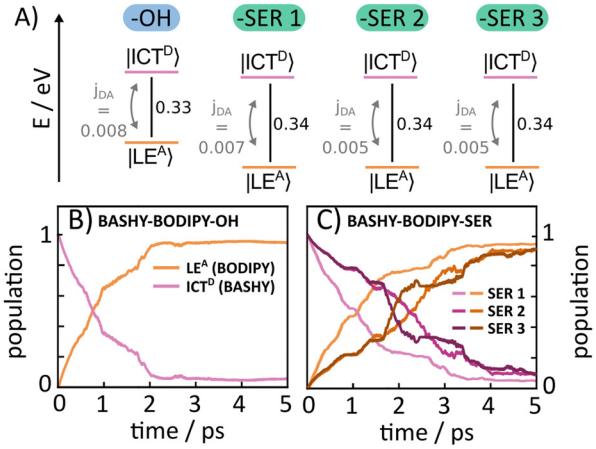

Fig. 6 (A) Schematic illustration of the electronic Hamiltonian of the two dyads **BASHY–BODIPY–OH** and **BASHY–BODIPY–SER** as well as the three considered conformations **–SER1**, **–SER2** and **–SER3**. The time-dependent diabatic population of the two included $|ICT^D\rangle$ (pink) and $|LE^A\rangle$ (orange) states for **BASHY–BODIPY–OH** (B) and the three different **BASHY–BODIPY–SER** conformations (C) is depicted for a simulation time of 5 ps. They are extracted from a full-dimensional ML-MCTDH propagation.

The models for all different conformations were parameterized based on the ground state equilibrium geometries and normal mode analyses complemented by excited state gradients. Fig. 6A displays a summary of the electronic Hamiltonian for all four conformations highlighting the slight differences between the two dyads and the conformations while Fig. 6B and C show the time-evolving diabatic populations of the ICT^D and LE^A states for **BASHY–BODIPY–OH** (B) and **BASHY–BODIPY–SER** (C), respectively. In comparison to the very fast coherent transfer of the previously investigated **RHO–BODIPY** dyad,[47] both systems, including **BASHY** as the donor moiety, feature a much slower process leading up to a timescale of 1–3 ps for the decay to the acceptor state rather than the 300 fs EET occurring in **RHO–BODIPY–OH**. The slight differences between the **–OH** and **–SER** based dyads can be reconciled with the slightly smaller ΔE and slightly higher coupling j_{DA} displayed by **BASHY–BODIPY–OH**. A similar line of reasoning can be applied to **–SER1**. As the **–SER2** and **–SER3** conformations do not display any differences in terms of their electronic Hamiltonian, the small discrepancies between them can be attributed primarily to the variation in their vibronic couplings. Table 3 gives an overview of the electronic couplings j_{DA}, the energy difference ΔE for the considered orientations, the respective torsional angle θ describing the rotation around the linker as well as the timescales of the population transfer represented by an approximate exponential decay rate. In contrast to the ultrafast, coherent EET step observed in ref. 47 for the **RHO–BODIPY** system, the **BASHY–BODIPY** dyads are closer to a quasi-kinetic regime where coherence builds up and decays transiently, while the overall decay appears irreversible (see Fig. S15, ESI†).

The discrepancy between the dyads including **RHO** and **BASHY** can be attributed to the greater energy separation

Open Access Article. Published on 14 February 2025. Downloaded on 2/20/2026 7:53:16 AM.
This article is licensed under a Creative Commons Attribution 3.0 Unported Licence.

Table 3 Total number of normal modes, orientation of θ, electronic coupling j_{DA}, ΔE as well as an indication for the EET timescale for all considered geometries. The decay rate τ_{EET} was obtained from an approximate exponential fit of the donor populations of Fig. 6 *i.e.*, $P_D(t) = A\exp\left(-\frac{t}{\tau_{EET}}\right)$

Molecule	N_{vib}	θ (°)	j_{DA} (eV)	ΔE (eV)	τ_{EET} (ps)
BASHY–BODIPY–OH	264	17.5	0.008	0.33	1.2
BASHY–BODIPY–SER1	339	−10.4	0.007	0.34	1.7
BASHY–BODIPY–SER2	339	169.2	−0.005	0.34	3.1
BASHY–BODIPY–SER3	339	266.7	−0.005	0.34	3.1

between the two states and the magnitude of the electronic coupling. Typical ratios for the **BASHY–BODIPY** system are $j_{DA}/\Delta E \sim 10^{-2}$, *i.e.* an order of magnitude smaller than in the **RHO–BODIPY** system, resulting in correspondingly larger transfer times. Despite the differences between the **RHO** and **BASHY** based dyads, the observed time scales extracted from the LVC description align well with the experimental results for the **BASHY–BODIPY** systems, as the timescales observed in the time-resolved spectroscopic measurements for **BASHY–BODIPY–OH** and **BASHY–BODIPY–SER** lie in the ps range as well.

2.4 Beyond the LVC description: potential energy surface scans

Despite the fact that the time scales of the energy transfer are adequately described by LVC dynamics, this description predicts a nearly complete EET for all **BASHY–BODIPY** dyads, contrary to the experimental observations where the transfer appears incomplete in the case of the **–OH** substituted dyad. The reason for the discrepancy most likely lies in the LVC approximation, which represents the potential energy surfaces within a shifted harmonic oscillator model, constructed around the FC geometry. This becomes manifested in a comparison of the theoretical reorganization energies obtained from the LVC parametrization with the experimental Stokes shift of the system. The reorganization energy of the **BASHY** fragment is obtained from the LVC model as $\lambda_D = 0.25$ eV, while λ_A is much smaller (see Section 2.3), such that the energy gap $\Delta E > \lambda$ throughout. In contrast, in the experimental steady-state spectrum of **BASHY**, the Stokes shift in DMSO measures approximately 0.4 eV. As the Stokes shift exceeds the initial energetic offset of around 0.3 eV between the S_1 and S_2 state, an interchange of the two states seems to occur during the measurement. The lower reorganization energy from the LVC parametrization cannot capture this so that the **BASHY**-centered state remains the higher lying state throughout. This may be one of the reasons why the LVC dynamics do not predict any difference between the dyad without and with LG, whereas the experimental steady-state and time-resolved experiments demonstrate a clear difference. The aforementioned disparity in the fluorescence properties of the dyad with and without the LG are evidenced in the previously investigated **RHO** based dyad as well. The markedly elevated fluorescence observed upon the cleavage of the leaving group enables its utilization, *e.g.*, in 2P fluorescence microscopy.[55]

To further analyze the difference from a theoretical viewpoint, rigid scans between the FC geometry and the optimized state geometries on the **BASHY** and **BODIPY** fragments were conducted. The scan coordinates X_1 and X_2 in Fig. 7 follow the

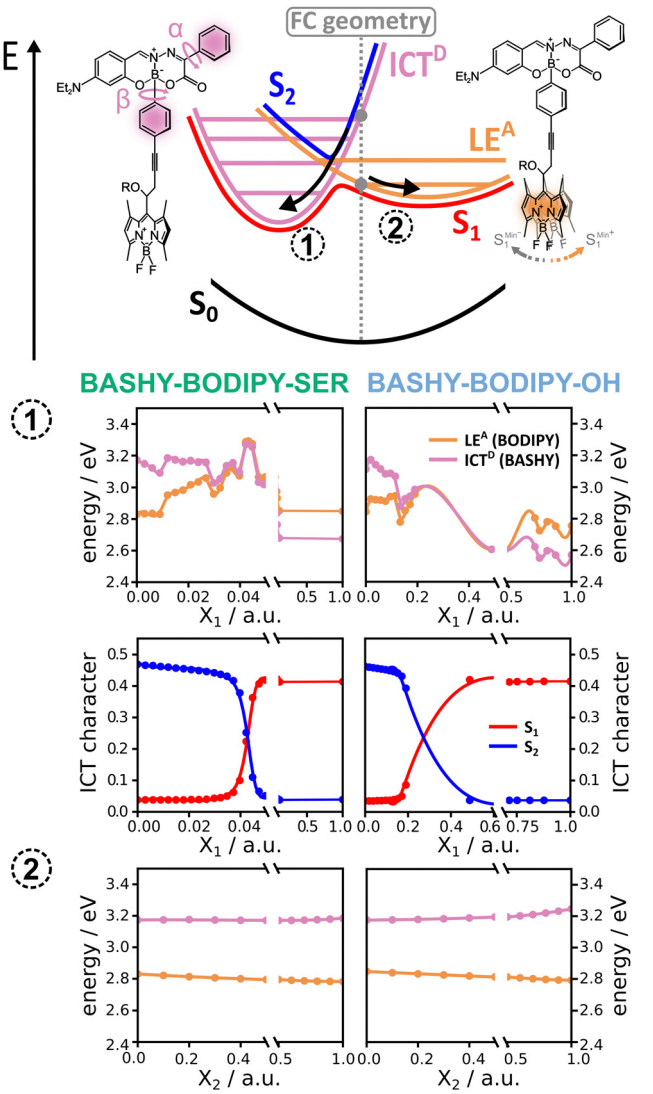

Fig. 7 Potential pathways within the **BASHY–BODIPY** dyads after initial photoexcitation. The PESs of the **BASHY**-centered state as well as the **BODIPY**-centered state are indicated *via* the pink and orange solid lines. Investigated pathways are flagged with the respective number in the schematic depiction of harmonic potentials above. Pathway 1 refers to the relaxation within the **BASHY**-centered ICT state that is initially excited. Potentials are obtained *via* a rigid scan following the gradient from the FC point to the S_2 state minimum geometry. This is referred to as scanning coordinate X_1. The evolution of the ICT character of the adiabatic S_1 and S_2 states is indicated in red and blue, respectively. For this analysis the **BASHY–BODIPY** dyads are divided into three sub-fragments of **BASHY**, the bridge and the **BODIPY** fragment. A more detailed definition of the ICT character as well as the exact partitioning of the **BASHY** fragment employed in the TheoDORE analysis can be found in the ESI.† Pathway 2 displays the relaxation to the S_1 state minimum along the scanning coordinate X_2. As the scanning coordinates of each panel correspond to the motion on the respective dyad moiety, these motions are included in the schematic depiction of potentials.

This journal is © the Owner Societies 2025

Open Access Article. Published on 14 February 2025. Downloaded on 2/20/2026 7:53:16 AM.
This article is licensed under a Creative Commons Attribution 3.0 Unported Licence.

gradient between the FC point and the respective LE^A or ICT^D state minimum, where one increment is normalized to the total displacement of atoms. Under the assumption that the step size between the scan points is reasonably small, following the gradient approximates the minimum energy pathway (MEP). The starting geometry (X = 0) is referring to the FC geometry, while the final geometries (X = 1) represent the optimized excited state geometries of the ICT^D and LE^A state, respectively (corresponding to pathway 1 *vs.* pathway 2). The scan reveals a reorganization energy for the ICT^D state, as the difference between the energies at X_1 = 0 and X_1 = 1, of approximately 0.5 eV, which is in reasonable agreement with the experimental Stokes shift. The elevated reorganization energy may facilitate pathway 1, as illustrated in Fig. 7. However, one should keep in mind that the actual dynamics does not follow the MEP since vibrational relaxation is not expected to be immediate.

A comparison of pathway 1 for the two dyads in Fig. 7 reveals that the crossing for **BASHY–BODIPY–SER** is situated closer to the FC point than that for **BASHY–BODIPY–OH**. Additionally, the slope of the PES for the dyad without leaving group (right hand side in Fig. 7) suggests a smooth transition towards the ICT^D geometry. The PES for the dyad with leaving group (left hand side in Fig. 7), on the other hand, displays a shallower slope enabling a redirection to the **BODIPY**-centered state. Both are in agreement with experimental findings.

A projection of the effective X_1 scanning coordinate onto molecular coordinates reveals two primary molecular movements, *i.e.*, the dihedral rotations around the respective benzyl substituents, denoted α and β in Fig. 7. Here, α corresponds to the rotation of the α-keto acid benzyl substituent relative to the extended π-system, while β corresponds to the dihedral rotation around the benzyl-linker forming the connection to the **BODIPY** moiety. In **BASHY–BODIPY–SER**, these two rotations act in an almost strictly sequential way, where the planarization of α is dominant before reaching the crossing, and the β rotation dominates after passage of the crossing. In contrast, the α rotation is significantly slower in **BASHY–BODIPY–OH** and continues to evolve after the crossing, together with the β rotation. Additional details can be found in Fig. S9 of the ESI.†

While both states are termed localized states in the sense that they are strictly localized on either fragment, the intra-fragment ICT character of the **BASHY**-centered state can be analyzed as shown in Fig. 7. The S_2 state (localized on **BASHY**) clearly shows an ICT character in the beginning, whereas the S_1 state (localized on **BODIPY**) exhibits no ICT character. Along the scan, the ICT character of the two states gradually shifts and swaps in the vicinity of the crossing.

In addition to the LVC dynamics and the investigation of the excited state PESs, absorption and emission spectra are simulated to model the emission of the equilibrium formed in **BASHY–BODIPY–OH**. The vibronic absorption and emission spectra can be obtained *via* the corresponding autocorrelation function.[48,56,57] The cross-section in the case of the absorption is computed employing the initial condition $\psi_g(0)$ of the ground state, while for the emission cross-section, the initial condition $\psi_e(0)$ is obtained *via* relaxation in the excited states. $\psi_e(0)$ can involve a superposition of $|LE^A\rangle$ and $|ICT^D\rangle$ depending on the respective energy difference ΔE and the coupling strength j_{DA}. The emission spectrum is then obtained as[56]

$$\sigma_{em}(\omega) = \frac{2\omega^3}{3\pi\hbar c^3}\int_{-\infty}^{\infty} dt \langle\psi_e(0)|\psi_e(t)\rangle e^{\left(-i\left(E-E_{0,e}\right)t/\tau_{em}\right)} \quad (3)$$

where τ_{em} acts as the damping time yielding a Lorentzian spectral envelope. The vibronic absorption spectra of **BASHY** as well as **BODIPY** can be found in Fig. S16 in the ESI† and display a fine structure matching the experimental ones given in Fig. 1. The phenomenological damping time τ_{em} is set to be 7 fs for the emission spectra shown in Fig. 8. All simulated spectra are shifted in order to match their experimental counterpart. In view of the importance of the ICT character of the **BASHY**-centered state $|ICT^D\rangle$ in the case of **BASHY–BODIPY–OH** the offset between the two involved singlet states is chosen as either 0.2 eV or 0.1 eV yielding coherent superpositions with an occupation of either 60% or 90% for the initially populated **BASHY**-centered $|ICT^D\rangle$ state. This results in an emission spectrum displaying intensities at both, the **BASHY** as well as the **BODIPY** wavelength (see Fig. 8B). The experimental steady-state emission of **BASHY–BODIPY–OH** seems to resemble a mean of the ratios of 10 : 90 and 40 : 60 for the state population of $|LE^A\rangle : |ICT^D\rangle$, thus attesting to the incomplete EET in the case of an absent LG. As the ICT character of the **BASHY** fragment, as previously discussed, is less important in the case of **BASHY–BODIPY–SER** no relaxation of the $|ICT^D\rangle$ state is assumed, yielding an emission spectrum resembling the isolated **BODIPY** fragment (see Fig. 8A). The obtained emission spectra in both cases are in good agreement with the experimental steady-state spectra, thus further corroborating the importance of the ICT character for **BASHY–BODIPY–OH** in comparison to **BASHY–BODIPY–SER**.

To further look into the behavior of **BASHY–BODIPY–OH** temperature-dependent fluorescence experiments were conducted for both dyads to examine whether the equilibrium between $|ICT^D\rangle$ and $|LE^A\rangle$ can be manipulated in favor of a

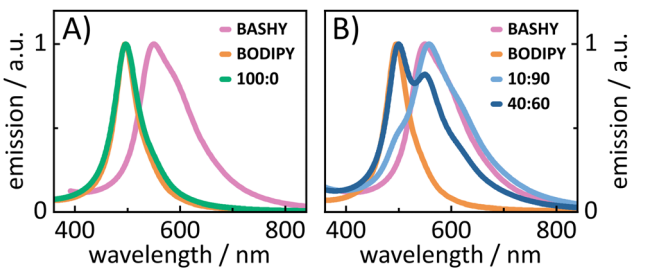

Fig. 8 Panel (A) shows the modeled emission spectra of **BASHY**, **BODIPY** and **BASHY–BODIPY–SER**, normalized and shifted in accordance to the experimental steady-state fluorescence spectra. ΔE is chosen according to the calculated energy offset of 0.34 eV, while the electronic coupling j_{DA} is 0.007 eV. The state population of $|LE^A\rangle$ and $|ICT^D\rangle$ is indicated as a ratio. Panel (B) displays the modeled emission spectra of **BASHY**, **BODIPY** and **BASHY–BODIPY–OH** accordingly. Here, two different scenarios are investigated, with a ΔE of either 0.1 eV or 0.2 eV and a coupling j_{DA} of 0.01 eV resulting in different ratios of state populations indicated in light blue and dark blue, respectively.

Open Access Article. Published on 14 February 2025. Downloaded on 2/20/2026 7:53:16 AM.
This article is licensed under a Creative Commons Attribution 3.0 Unported Licence.

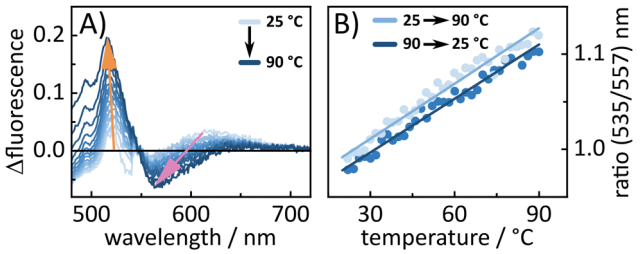

Fig. 9 Temperature-dependent fluorescence experiment of **BASHY–BODIPY–OH**. (A) The differential change of the fluorescence shape from 25 to 90 °C in 5 °C steps. (B) The same and additionally the reverse experiment from 90 back to 25 °C. Thereby, the ratio of the **BODIPY** peak at 535 nm and the **BASHY** peak at 557 nm are plotted against the temperature. The reverse experiment proofs that the temperature-induced changes are reversible.

transfer towards the **BODIPY**-centered state. In fact, for **BASHY–BODIPY–OH**, we clearly see that an increase in temperature leads to a shift towards a **BODIPY**-like fluorescence (Fig. 9A). This temperature-induced fluorescence change is reversible, when the temperature is decreased again (Fig. 9B), further validating the existence of an equilibrium between the $|LE^{A}\rangle$ and $|ICT^{D}\rangle$ state. The same experiment was repeated for **BASHY–BODIPY–SER**, however, the fluorescence shape did not show any significant change.

In contrast, **BASHY–BODIPY–SER** appears to decompose at elevated temperatures, resulting in an irreversible alteration of its photophysical properties, particularly its fluorescence (Fig. S22, ESI†). Thus, a comparison of the absorption spectra before and after the temperature excursion experiment revealed the decomposition of the caging dyad in the course of the experiment.

2.5 Effective Förster resonance energy transfer rates

As previously shown the transient absorption measurements and subsequent lifetime density analysis reveal EET timescales of a few picoseconds for both dyads, aligning well with the calculated values from the quantum dynamical simulations. Due to the slow timescale of the quasi-kinetic EET (see Section 2.3), we will explore a more approximate, effective Förster resonance energy transfer (FRET) description in this section. Given the spatial extension of the chromophores and the center-of-mass separation between the chromophores of 1.19 nm, the accuracy of the FRET model and its parameters may be compromised as previously discussed in the literature.[58–60] Due to these limitations, we will adopt a more phenomenological treatment of FRET to mainly evaluate whether the FRET model can account for the observed differences between the two dyads.

FRET depends on many characteristic parameters such as chromophore distance, dipole orientation and spectral overlap. In the following, these parameters and their contributions to the FRET efficiencies will be briefly discussed. A more detailed explanation of the FRET theory and its parameters is given in the ESI.† The major difficulty in these calculations is how to distinguish between the two dyads, given that they are structurally almost identical despite the LG. For example, due to the similarity of the systems, the chromophore distance (1.19 nm) is identical and can be excluded as a reason for the divergent FRET efficiencies. Also, the quite rigid geometry, owing to the alkyne linker between the chromophore units, is similar in both dyads. The rigidity of the dyads makes a dynamic averaging of the orientation factor κ^2, usually done for many biomolecular systems, unreasonable. Thus, for an accurate determination of κ^2, the different rotamer conformations and their Boltzmann distribution (see the ESI† for more details) were examined, resulting in an average κ^2 value of 0.48 for both dyads. Thus, the chromophore orientation is seemingly not responsible for the different energy transfer efficiencies. The overlap integral J, based on the overlap between the donor emission and the acceptor absorbance, would theoretically be the same for both dyads as well due to the identical chromophore units. However, the previously discussed steady state and transient absorption measurements showed significant differences in their emission behavior, which can in turn impact the EET. Specifically, **BASHY–BODIPY–OH** exhibits a pronounced ICT stabilization of its **BASHY** chromophore, while **BASHY–BODIPY–SER** shows no significant ICT relaxation. To consider these differences for the calculation of J, the fluorescence of **BASHY** in DMSO serves as a good approximation for **BASHY–BODIPY–OH**, while the fluorescence of **BASHY** in toluene is more appropriate for **BASHY–BODIPY–SER**, as it reflects **BASHY**'s initial fluorescence without any ICT stabilization. As illustrated in the upper panel of Fig. 10, the presence or

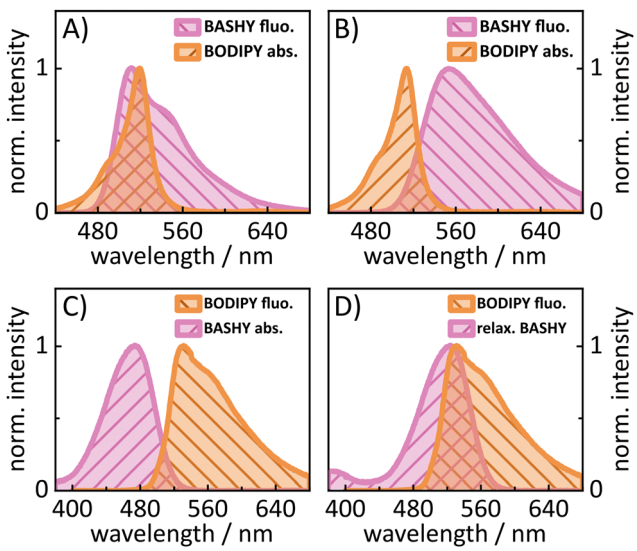

Fig. 10 Spectra used for the calculation of the overlap integral in different cases. The upper panel shows the overlap between **BASHY**'s fluorescence and **BODIPY**'s absorbance, indicating the forward-EET (A) without and (B) with CT evolution in **BASHY**. For this purpose, the fluorescence of **BASHY** in toluene was used for (A), representative for the initial **BASHY** fluorescence without any CT characteristic. On the other hand, for (B) the actual **BASHY** fluorescence in DMSO was used. The lower panel shows the overlap between **BODIPY**'s fluorescence and **BASHY**'s absorbance to account for the possibility of a back-EET. While for (C) the actual steady-state absorption spectrum of **BASHY** was used, the same spectrum was shifted by 40 nm in (D) to account for the relaxed potential energy surface of **BASHY** during charge transfer stabilization.

This journal is © the Owner Societies 2025

Open Access Article. Published on 14 February 2025. Downloaded on 2/20/2026 7:53:16 AM.
This article is licensed under a Creative Commons Attribution 3.0 Unported Licence.

Table 4 Calculated FRET parameters and efficiencies for the different cases illustrated in Fig. 10

Case	J	R_0 (nm)	E_{FRET} (%)	τ_D (ns)	k_T (s^{-1})	τ_{FRET} (ps)
A	1.38^{15}	4.65	99.9	2.4	1.5^{12}	0.7
B	2.49^{14}	2.77	99.3	0.7	2.3^{11}	4.3
C	9.45^{13}	2.36	98.4	2.1	2.9^{10}	34
D	3.21^{15}	4.24	99.9	2.1	9.7^{11}	1.0

Further details on the calculation of FRET rates are provided in the ESI. The transfer rates k_T were determined using the donor lifetimes τ_D, which were all taken from TCSPC measurements, expect for case B, where the lifetime was within the timescale of our transient absorption setup.

absence of the ICT relaxation significantly impacts the overlap integral. In the absence of an ICT stabilization of the **BASHY** chromophore (Fig. 10A), the overlap with **BODIPY**'s absorbance is larger by almost one order of magnitude compared to the case with an ICT fluorescence of **BASHY** (Fig. 10B), as can be seen by the calculated values in Table 4. Even though the overlap integrals differ significantly, both cases result in nearly 100% FRET efficiencies, E_{FRET}. This is due to the short distance (1.19 nm) between the centers of mass of the chromophores, which is way smaller than the calculated Förster radii R_0 in Table 4. Since these results do not explain the observed difference between the two dyads, the possibility of a back-EET from **BODIPY** to **BASHY** was considered as well (see lower panel of Fig. 10C), as the short distance and significant overlap between the spectra makes it nearly as efficient as the forward-EET (compare Table 4). However, in contrast to the FRET efficiencies, the energy transfer rates k_T differ significantly in their magnitudes and thus the equilibrium constant between forward- and back-EET will determine the directional preference of the EET, which will be discussed in the following for different scenarios. For **BASHY–BODIPY–SER**, using the ratio of the forward rate A and backward rate C, where no ICT stabilization of **BASHY** is involved, results in an equilibrium constant of 52, indicating a clear preference for the forward-EET in **BASHY–BODIPY–SER**. For **BASHY–BODIPY–OH**, considering the ICT stabilization by using the transfer rate of B for the forward-EET and the transfer rate of C for the backward-EET, leads to a significant drop of the equilibrium constant to 8. Comparing both scenarios, the equilibrium constant decreases as the ICT character of **BASHY** strengthens, meaning the forward-EET slows down. However, it does not fully align with the experimental data, which suggest at least a 50 : 50 distribution, corresponding to an equilibrium constant of 1.

This discrepancy arises because steady-state spectra alone cannot fully account for the excited-state dynamics in the dyads. For instance, the reverse energy transfer is calculated using **BASHY**'s steady state absorption without considering the relaxed potential energy surface, which would cause a stronger redshift in its absorption and likely a greater overlap integral with **BODIPY**'s fluorescence. Therefore, the reverse energy transfer rate might be higher than anticipated. For this instance, a forth case (Fig. 10D) was introduced, where the steady-state absorption spectrum of **BASHY** (shown in Fig. 10C) was shifted by 40 nm to mimic the relaxed potential of **BASHY**. Indeed, this leads to a greater overlap integral of **BODIPY**'s fluorescence and **BASHY**'s absorption (see Table 4). Calculating the equilibrium constant now using the case (Fig. 10B) for the forward-EET and case (Fig. 10D) for the back-EET, leads to a value of 0.25, a clear preference for the back-EET by four times. These scenarios explain how the stronger ICT stabilization of the **BASHY** chromophore in **BASHY–BODIPY–OH** leads to an incomplete forward-EET. Furthermore, these results imply that the back-EET is preferred in the case of a relaxed **BASHY** potential, meaning that a direct **BODIPY** excitation will not lead to any significant population of **BASHY**. This additionally explains why a back-EET is not directly observable in a transient absorption measurement with a direct excitation of the **BODIPY** chromophore. A comparison of the calculated FRET lifetimes in Table 4 with the experimental results from the transient absorption measurements and the calculated values from the quantum dynamical analysis in Table 3 reveals that the FRET calculations fall within a reasonable range. In particular, the FRET calculations of the forward-EET lifetimes τ_{FRET}, which range from 0.7–4.3 ps, depending on the extent of the ICT stabilization, align well with the experimental and theoretical results of a few picoseconds. In contrast, the back-EET lifetime from **BODIPY** to an ICT-stabilized **BASHY** is calculated to be 1 ps, placing it into the same timescale as the forward-EET. This estimated temporal overlap of forward- and backward-EET makes a clear assignment of a reverse EET in the transient absorption spectra difficult. Despite using several approximations for the calculation of the FRET rates and lifetimes, these calculations are reasonable and in good agreement with the previous results. Additionally, the kinetic nature of the EET process within the dyads and its strong dependence on the ICT stabilization of the **BASHY** chromophore could be further confirmed.

2.6 Schematic models of excited-state pathways

Based on the experimental and theoretical results, two possible models (see Fig. 11) are outlined in order to visualize the special characteristics of the two dyads. After excitation of the **BASHY** chromophore, there are two possible pathways for the distribution of the excitation energy. It either remains

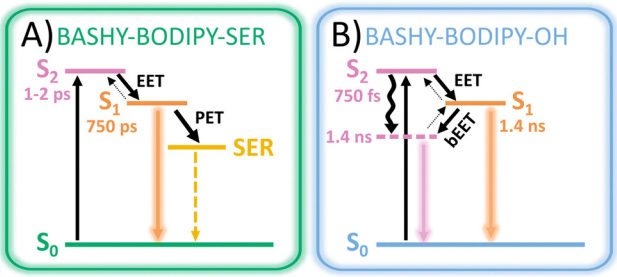

Fig. 11 Schematic models featuring all possible photophysical pathways within (A) **BASHY–BODIPY–SER** and (B) **BASHY–BODIPY–OH**. Arrows in two directions indicate the existence of equilibria for certain processes, whereby the bold arrows mark the dominant direction.

Open Access Article. Published on 14 February 2025. Downloaded on 2/20/2026 7:53:16 AM. This article is licensed under a Creative Commons Attribution 3.0 Unported Licence.

within the excited **BASHY** chromophore and enables the solvent-guided relaxation due to the ICT character or an energy transfer to the **BODIPY** chromophore can take place. The latter is the dominant pathway in **BASHY–BODIPY–SER**, while in **BASHY–BODIPY–OH** both pathways are accessible to a certain degree.

In **BASHY–BODIPY–SER** the EET (~1–2 ps) from **BASHY** to **BODIPY** is the dominant pathway to an extent, in that no relaxation in the **BASHY**-centered state is noticeable. Since there is no significant lowering of the **BASHY** state, the back-EET (bEET) from **BODIPY** to **BASHY** is less likely as discussed within the perspective of a rate process. Thus, the main dynamics take place from **BODIPY**, where various relaxation processes are involved. Besides the fluorescence from **BODIPY**, PET to **SER** seems to be a dominant deactivation channel as noticeable by the reduced fluorescence quantum yield (~10%) and the shortened excited state lifetime (~750 ps). Uncaging as the most important process in a photocage will be discussed in the upcoming section.

In **BASHY–BODIPY–OH** on the other hand, the EET (~750 fs) from **BASHY** to **BODIPY** strongly competes with the relaxation process within the **BASHY** chromophore. As the state ordering changes in the process of the relaxation of the ICT **BASHY** state, the transfer at some point will change direction as well. Coincidentally with the ICT relaxation, the bEET from **BODIPY** to the relaxed **BASHY** PES takes over, which also increases the **BASHY** population. Hence, the excitation energy is more likely to remain within the **BASHY** chromophore as the ICT relaxation plays a significant role. Since both chromophore states are possibly populated, the **BASHY–BODIPY–OH** dyad shows mixed dynamics, resulting in combined spectroscopic properties from both chromophore units. Hence, the excited-state lifetime (~1.4 ns) lies in between the individual chromophores.

The equilibrium of the EET can be influenced by temperature as we have shown for **BASHY–BODIPY–OH** (Fig. 9). In addition to the temperature dependence, the PES landscape could also be influenced by solvent molecules as their proticity, polarity and viscosity cannot only affect the amount of ICT relaxation, but also its timescale and in turn the equilibrium directly. Indeed, steady-state spectra suggest a high solvent dependency even for **BASHY–BODIPY–SER**, where the EET efficiency is slightly reduced in a more polar solvent (MECN/water mixture) as notable from the significant increase in **BASHY** fluorescence (Fig. S18, ESI†).

2.7 Uncaging experiments

Finally, after extensive analysis of the energy transfer, the uncaging ability of the **BASHY–BODIPY–SER** dyad was investigated. Since for most photocages, it is assumed that the uncaging proceeds *via* formation of a cation followed by hydroxylation through a protic solvent,[44] a DMSO/water (9 : 1) mixture was used. The hydroxylation of the cation would result in **BASHY–BODIPY–OH** as the main photoproduct. As both dyads exhibit such distinct fluorescence spectra, it was assumed that the uncaging progress could be tracked by the changes in fluorescence. Therefore, fluorescence spectra were recorded after a certain time of illumination. As seen in (Fig. 12), **BASHY–BODIPY–SER** changes both in its absorption and fluorescence. The absorption changes (Fig. 12A) mainly result from the bleaching of the **BODIPY** photoproduct which is common for **BODIPY** photocages.[44] However, there are no further photoproducts distinguishable from the absorption spectra.

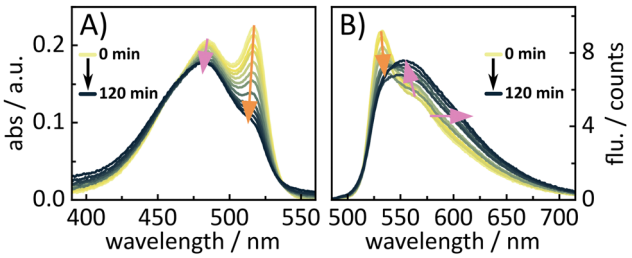

Fig. 12 Illumination experiment of **BASHY–BODIPY–SER** to investigate the uncaging progress by changes in the (A) absorption and (B) fluorescence.

As expected, the fluorescence spectra (Fig. 12B) show more significant changes during the illumination experiment. While the fluorescence of **BODIPY** at 532 nm decreases, the fluorescence of **BASHY** at 554 nm starts to increase and extends further into the red. To further validate these changes, the fluorescence quantum yields were recorded before and after the experiment since **BASHY–BODIPY–SER** has a lower fluorescence quantum yield than **BASHY–BODIPY–OH**. Indeed, the fluorescence efficiency also increases from 2.2% to 5.8%. It should be noted that the fluorescence quantum yields are significantly reduced in the DMSO/water mixture due to the stabilization of the ICT state. But the overall tendency of the lower fluorescence efficiency of **BASHY–BODIPY–SER** seems to be preserved in more polar solvents as well. Overall, the changes in fluorescence are useful to follow the uncaging progress, but they cannot be used to determine the uncaging quantum yield quantitatively. Therefore, illumination experiments were conducted in the IR to track the CO_2 release from **BASHY–BODIPY–SER**. CO_2 should be formed due to decarboxylation of the carbamate linker during the uncaging process. An uncaging quantum yield of 0.03% was determined from the CO_2 release (Fig. S23, ESI†). Small changes of two peaks in the carbamate region were observed as well, but these peaks are covered by the strong solvent interactions nearby. These interactions led to a strong rise of solvent associated bands which in turn presumably masked many of the molecule's vibrations. Overall, the uncaging efficiency of the dyad certainly leaves space for further optimization by better photocage chromophores. For example a better **BODIPY** photocage with more rigid[12] and/or halogenated substituents[44] can lead to improved uncaging efficiencies as seen in our recent publication.[27]

3 Conclusion

In conclusion, we designed an intramolecular dyad based on a **BASHY** fluorophore and **BODIPY** photocage as an EET system

Open Access Article. Published on 14 February 2025. Downloaded on 2/20/2026 7:53:16 AM. This article is licensed under a Creative Commons Attribution 3.0 Unported Licence.

that features greatly superior 2-photon excitability as compared with the **BODIPY** photocage by itself. Interestingly, it turned out that the leaving group is an active player in the EET process. Notably, we showed that the excited state PES landscape is sensitive to the addition of a LG, which highly boosts the EET compared to the dyad without LG. Thus, the leaving group can be used to control the energy transfer and in turn the fluorescence output.

Since other leaving groups lead to a similar preference of the EET pathway, the present observations could lead to a new design concept. This concept allows a significant fluorescence read-out upon uncaging, which should make it attractive for microscopic applications, which usually rely on fluorescence quenchers as LGs to restore the fluorescence upon uncaging. Furthermore, we showed that an antenna with a strong ICT character can be exploited to control the EET efficiency by external factors such as temperature or solvent. This kind of system could be useful for dynamical applications where environment sensitivity is crucial.

At the molecular level, we have shown that the changes of the potential energy surface in the presence of the LG are subtle and non-local. These changes translate to differences in the approach towards the non-adiabatic crossing, along with differences in the participation of two dihedral angles in the minimum energy path. Both aspects shift the balance between the EET pathway and relaxation in the donor ICT state. Certain key vibrations likely have to be active to induce efficient vibrational relaxation in the donor state. These issues will be fully explored in follow-up work where the dynamics at the non-adiabatic crossing will be investigated.

Author contributions

Yagmur Aydogan-Sun: writing – original draft, data curation, investigation, methodology, visualization. Maximiliane Horz: writing – original draft, data curation, investigation, methodology, visualization. Rebekka Weber: investigation, resources, data curation, methodology. Myron Heinz: data curation. Markus Braun: validation. Alexander Heckel: supervision, funding acquisition, conceptualization. Irene Burghardt: supervision, writing – review and editing, supervison, funding acquisition, conceptualization. Josef Wachtveitl: supervision, writing – review and editing, supervison, funding acquisition, conceptualization.

Data availability

Additional data supporting this article have been included as part of the ESI.† Furthermore, all raw and corrected data sets for this article are available at Goethe University Data Repository at **https://doi.org/10.25716/gude.031v-j4fc**.

Conflicts of interest

There are no conflicts to declare.

Acknowledgements

It is a great pleasure to dedicate this article to Christel Marian on the occasion of her 70th birthday. Furthermore, we gratefully acknowledge Deutsche Forschungsgemeinschaft (DFG) for the funding of our research training group ''CLiC'' (GRK 1986, Complex Light-Control). We express our sincere gratitude to the European Union for funding our TCSPC laser system through the European Regional Development Fund as part of the Union's response to the COVID-19 pandemic – REACT-EU, IWB-EFRE-Programm Hessen, #20008794.

Notes and references

1 P. Seyfried, L. Eiden, N. Grebenovsky, G. Mayer and A. Heckel, *Angew. Chem., Int. Ed.*, 2017, **56**, 359–363.
2 N. Klöcker, F. P. Weissenboeck, M. van Dülmen, P. Špaček, S. Hüwel and A. Rentmeister, *Nat. Chem.*, 2022, **14**, 905–913.
3 V. Gatterdam, T. Stoess, C. Menge, A. Heckel and R. Tampé, *Angew. Chem., Int. Ed.*, 2012, **51**, 3960–3963.
4 C. Bier, D. Binder, D. Drobietz, A. Loeschcke, T. Drepper, K.-E. Jaeger and J. Pietruszka, *Synthesis*, 2016, 42–52.
5 S. B. Cambridge, D. Geissler, F. Calegari, K. Anastassiadis, M. T. Hasan, A. F. Stewart, W. B. Huttner, V. Hagen and T. Bonhoeffer, *Nat. Methods*, 2009, **6**, 527–531.
6 L.-M. Herzig, I. Elamri, H. Schwalbe and J. Wachtveitl, *Phys. Chem. Chem. Phys.*, 2017, **19**, 14835–14844.
7 I. Elamri, C. Abdellaoui, J. K. Bains, K. F. Hohmann, S. L. Gande, E. Stirnal, J. Wachtveitl and H. Schwalbe, *J. Am. Chem. Soc.*, 2021, **143**, 10596–10603.
8 G. He, M. He, R. Wang, X. Li, H. Hu, D. Wang, Z. Wang, Y. Lu, N. Xu, J. Du, J. Fan, X. Peng and W. Sun, *Angew. Chem., Int. Ed.*, 2023, **62**, e202218768.
9 E. M. Digby, S. Ayan, P. Shrestha, E. J. Gehrmann, A. H. Winter and A. A. Beharry, *J. Med. Chem.*, 2022, **65**, 16679–16694.
10 A. M. Smith, M. C. Mancini and S. Nie, *Nat. Nanotechnol.*, 2009, **4**, 710–711.
11 R. Weinstain, T. Slanina, D. Kand and P. Klán, *Chem. Rev.*, 2020, **120**, 13135–13272.
12 P. Shrestha, K. C. Dissanayake, E. J. Gehrmann, C. S. Wijesooriya, A. Mukhopadhyay, E. A. Smith and A. H. Winter, *J. Am. Chem. Soc.*, 2020, **142**, 15505–15512.
13 A. Egyed, K. Németh, T. A. Molnár, M. Kállay, P. Kele and M. Bojtár, *J. Am. Chem. Soc.*, 2023, **145**, 4026–4034.
14 M. Klausen and M. Blanchard-Desce, *J. Photochem. Photobiol., C*, 2021, **48**, 100423.
15 E. B. Brown, J. B. Shear, S. R. Adams, R. Y. Tsien and W. W. Webb, *Biophys. J.*, 1999, **76**, 489–499.
16 M. Matsuzaki, G. C. R. Ellis-Davies, T. Nemoto, Y. Miyashita, M. Iino and H. Kasai, *Nat. Neurosci.*, 2001, **4**, 1086–1092.
17 V. Nikolenko, K. E. Poskanzer and R. Yuste, *Nat. Methods*, 2007, **4**, 943–950.
18 M. Pawlicki, H. Collins, R. Denning and H. Anderson, *Angew. Chem., Int. Ed.*, 2009, **48**, 3244–3266.

Open Access Article. Published on 14 February 2025. Downloaded on 2/20/2026 7:53:16 AM. This article is licensed under a Creative Commons Attribution 3.0 Unported Licence.

19 G. Bassolino, C. Nançoz, Z. Thiel, E. Bois, E. Vauthey and P. Rivera-Fuentes, *Chem. Sci.*, 2018, **9**, 387–391.
20 R. Klimek, M. Asido, V. Hermanns, S. Junek, J. Wachtveitl and A. Heckel, *Chem. – Eur. J.*, 2022, **28**, e202200647.
21 M. Klausen, V. Dubois, J.-B. Verlhac and M. Blanchard-Desce, *ChemPlusChem*, 2019, **84**, 589–598.
22 C. A. Hammer, K. Falahati, A. Jakob, R. Klimek, I. Burghardt, A. Heckel and J. Wachtveitl, *J. Phys. Chem. Lett.*, 2018, **9**, 1448–1453.
23 G. Ulrich, R. Ziessel and A. Harriman, *Angew. Chem., Int. Ed.*, 2008, **47**, 1184–1201.
24 P. Shrestha, D. Kand, R. Weinstain and A. H. Winter, *J. Am. Chem. Soc.*, 2023, **145**, 17497–17514.
25 F. M. F. Santos, J. N. Rosa, N. R. Candeias, C. P. Carvalho, A. I. Matos, A. E. Ventura, H. F. Florindo, L. C. Silva, U. Pischel and P. M. P. Gois, *Chem. – Eur. J.*, 2016, **22**, 1631–1637.
26 M. M. Alcaide, F. M. F. Santos, V. F. Pais, J. I. Carvalho, D. Collado, E. Pérez-Inestrosa, J. F. Arteaga, F. Boscá, P. M. P. Gois and U. Pischel, *J. Org. Chem.*, 2017, **82**, 7151–7158.
27 R. Weber, K. Chok, S. Junek, C. Glaubitz and A. Heckel, *Chem. – Eur. J.*, 2023, **29**, e202300149.
28 T. Kobayashi, T. Komatsu, M. Kamiya, C. Campos, M. González-Gaitán, T. Terai, K. Hanaoka, T. Nagano and Y. Urano, *J. Am. Chem. Soc.*, 2012, **134**, 11153–11160.
29 C. Xu and W. W. Webb, *J. Opt. Soc. Am. B*, 1996, **13**, 481.
30 F. M. F. Santos, Z. Domínguez, J. P. L. Fernandes, C. Parente Carvalho, D. Collado, E. Pérez-Inestrosa, M. V. Pinto, A. Fernandes, J. F. Arteaga, U. Pischel and P. M. P. Gois, *Chem. – Eur. J.*, 2020, **26**, 14064–14069.
31 M. J. Frisch, G. W. Trucks, H. B. Schlegel, G. E. Scuseria, M. A. Robb, J. R. Cheeseman, G. Scalmani, V. Barone, G. A. Petersson, H. Nakatsuji, X. Li, M. Caricato, A. V. Marenich, J. Bloino, B. G. Janesko, R. Gomperts, B. Mennucci, H. P. Hratchian, J. V. Ortiz, A. F. Izmaylov, J. L. Sonnenberg, D. Williams-Young, F. Ding, F. Lipparini, F. Egidi, J. Goings, B. Peng, A. Petrone, T. Henderson, D. Ranasinghe, V. G. Zakrzewski, J. Gao, N. Rega, G. Zheng, W. Liang, M. Hada, M. Ehara, K. Toyota, R. Fukuda, J. Hasegawa, M. Ishida, T. Nakajima, Y. Honda, O. Kitao, H. Nakai, T. Vreven, K. Throssell, J. A. Montgomery, Jr., J. E. Peralta, F. Ogliaro, M. J. Bearpark, J. J. Heyd, E. N. Brothers, K. N. Kudin, V. N. Staroverov, T. A. Keith, R. Kobayashi, J. Normand, K. Raghavachari, A. P. Rendell, J. C. Burant, S. S. Iyengar, J. Tomasi, M. Cossi, J. M. Millam, M. Klene, C. Adamo, R. Cammi, J. W. Ochterski, R. L. Martin, K. Morokuma, O. Farkas, J. B. Foresman and D. J. Fox, *Gaussian 16 Revision C.01*, Gaussian Inc., Wallingford CT, 2016.
32 T. Yanai, D. P. Tew and N. C. Handy, *Chem. Phys. Lett.*, 2004, **393**, 51–57.
33 F. Weigend and R. Ahlrichs, *Phys. Chem. Chem. Phys.*, 2005, **7**, 3297–3305.
34 F. Weigend, *Phys. Chem. Chem. Phys.*, 2006, **8**, 1057–1065.
35 S. Miertuš, E. Scrocco and J. Tomasi, *Chem. Phys.*, 1981, **55**, 117–129.
36 S. Miertuš and J. Tomasi, *Chem. Phys.*, 1982, **65**, 239–245.
37 J. L. Pascual-ahuir, E. Silla and I. Tuñon, *J. Comput. Chem.*, 1994, **15**, 1127–1138.
38 F. Plasser and H. Lischka, *J. Chem. Theory Comput.*, 2012, **8**, 2777–2789.
39 F. Plasser, *J. Chem. Phys.*, 2020, **152**, 084108.
40 F. Plasser, *THEODORE: A package for theoretical density, orbital relaxation, and exciton analysis*, 2019, **https://theodore-qc.sourceforge.net**.
41 J. Felicidade, F. M. F. Santos, J. F. Arteaga, P. Remón, R. Campos-González, H.-C. Nguyen, F. Nájera, F. Boscá, D. Y. W. Ng, P. M. P. Gois and U. Pischel, *Chem. – Eur. J.*, 2023, **29**, e202300579.
42 A. D. Laurent, B. Le Guennic and D. Jacquemin, *Theor. Chem. Acc.*, 2016, **135**, 173.
43 F. M. F. Santos, J. N. Rosa, N. R. Candeias, C. P. Carvalho, A. I. Matos, A. E. Ventura, H. F. Florindo, L. C. Silva, U. Pischel and P. M. P. Gois, *Chem. – Eur. J.*, 2016, **22**, 1631–1637.
44 T. Slanina, P. Shrestha, E. Palao, D. Kand, J. A. Peterson, A. S. Dutton, N. Rubinstein, R. Weinstain, A. H. Winter and P. Klán, *J. Am. Chem. Soc.*, 2017, **139**, 15168–15175.
45 M. Kawatani, M. Kamiya, H. Takahashi and Y. Urano, *Bioorg. Med. Chem. Lett.*, 2018, **28**, 1–5.
46 K. Aidas, C. Angeli, K. L. Bak, V. Bakken, R. Bast, L. Boman, O. Christiansen, R. Cimiraglia, S. Coriani, P. Dahle, E. K. Dalskov, U. Ekström, T. Enevoldsen, J. J. Eriksen, P. Ettenhuber, B. Fernández, L. Ferrighi, H. Fliegl, L. Frediani, K. Hald, A. Halkier, C. Hättig, H. Heiberg, T. Helgaker, A. C. Hennum, H. Hettema, E. Hjertenæs, S. Høst, I.-M. Høyvik, M. F. Iozzi, B. Jansík, H. J. Aa. Jensen, D. Jonsson, P. Jørgensen, J. Kauczor, S. Kirpekar, T. Kjærgaard, W. Klopper, S. Knecht, R. Kobayashi, H. Koch, J. Kongsted, A. Krapp, K. Kristensen, A. Ligabue, O. B. Lutnæs, J. I. Melo, K. V. Mikkelsen, R. H. Myhre, C. Neiss, C. B. Nielsen, P. Norman, J. Olsen, J. M. H. Olsen, A. Osted, M. J. Packer, F. Pawlowski, T. B. Pedersen, P. F. Provasi, S. Reine, Z. Rinkevicius, T. A. Ruden, K. Ruud, V. V. Rybkin, P. Sałek, C. C. M. Samson, A. S. de Merás, T. Saue, S. P. A. Sauer, B. Schimmelpfennig, K. Sneskov, A. H. Steindal, K. O. Sylvester-Hvid, P. R. Taylor, A. M. Teale, E. I. Tellgren, D. P. Tew, A. J. Thorvaldsen, L. Thøgersen, O. Vahtras, M. A. Watson, D. J. D. Wilson, M. Ziolkowski and H. Ågren, *Wiley Interdiscip. Rev.:Comput. Mol. Sci.*, 2014, **4**, 269–284.
47 M. Asido, C. Hamerla, R. Weber, M. Horz, M. S. Niraghatam, A. Heckel, I. Burghardt and J. Wachtveitl, *Phys. Chem. Chem. Phys.*, 2022, **24**, 1795–1802.
48 V. May and O. Kühn, *Charge and Energy Transfer Dynamics in Molecular Systems*, John Wiley & Sons, Ltd, 3rd edn, 2011.
49 H. Wang, *J. Phys. Chem. A*, 2015, **119**, 7951–7965.
50 M. Beck, A. Jäckle, G. Worth and H.-D. Meyer, *Phys. Rep.*, 2000, **324**, 1–105.
51 G. Worth, M. Beck, A. Jäckle and H.-D. Meyer, *MCTDH Package, Version 8.5.5*, Heidelberg University, 2016, **https://www.mctdh.uni-hd.de**.
52 H. Köuppel, W. Domcke and L. Cederbaum, *Adv. Chem. Phys.*, 1984, **57**, 59–246.

53 H. Tamura, R. Martinazzo, M. Ruckenbauer and I. Burghardt, *J. Chem. Phys.*, 2012, **137**, 22A540.
54 M. F. Iozzi, B. Mennucci, J. Tomasi and R. Cammi, *J. Chem. Phys.*, 2004, **120**, 7029–7040.
55 R. Weber, S. Junek and A. Heckel, *Chem. – Eur. J.*, 2023, **29**, e202300997.
56 D. J. Tannor, *Introduction to Quantum Mechanics: A Time-Dependent Perspective*, University Science Books, USA, 1st edn, 2007.
57 S. Mukamel, S. Abe and R. Islampour, *J. Phys. Chem.*, 1985, **89**, 201–204.
58 D. Beljonne, C. Curutchet, G. D. Scholes and R. J. Silbey, *J. Phys. Chem. B*, 2009, **113**, 6583–6599.
59 E. Yang, J. Wang, J. R. Diers, D. M. Niedzwiedzki, C. Kirmaier, D. F. Bocian, J. S. Lindsey and D. Holten, *J. Phys. Chem. B*, 2014, **118**, 1630–1647.
60 J. F. Galindo, V. M. Freixas, S. Tretiak and S. Fernandez-Alberti, *J. Phys. Chem. Lett.*, 2021, **12**, 10394–10401.

Open Access Article. Published on 14 February 2025. Downloaded on 2/20/2026 7:53:16 AM.
This article is licensed under a Creative Commons Attribution 3.0 Unported Licence.